



Enhanced electrocatalytic nitrate reduction through phosphorus-vacancy-mediated kinetics in heterogeneous bimetallic phosphide hollow nanotube array

Yihong Gao^a, Kunpeng Wang^a, Chao Xu^a, Hao Fang^a, Huili Yu^a, Hui Zhang^a, Shikuo Li^a, Chuanhao Li^b, Fangzhi Huang^{a,*}

^a School of Material Science and Engineering & School of Chemical and Chemical Engineering Anhui University, Hefei 230601, China

^b School of Environmental Science and Engineering, Sun Yat-sen University, Guangzhou 510006, China

ARTICLE INFO

Keywords:

Phosphorus vacancy
Nitrate reduction reaction
Eight-electron nine-proton reaction
Electrocatalysis system
Zn-NO₃ battery system

ABSTRACT

Electrocatalytic NO₃⁻ reduction reaction (NO₃RR) is of great significance in pollution treatment and energy conversion, and its core problem is how to realize rapid electron transfer and easy-to-adjust electronic structure to meet the needs of eight-electron nine-proton reaction. Vacancy engineering is considered as reasonable strategy to optimize the electronic structure, accelerate the kinetic process. Therefore, based on the strategy of doping-oxygen to induce the generation of phosphorus vacancy, heterogeneous bimetallic phosphide CoP-Ni₂P with controllable phosphorus vacancy was successfully constructed. Theoretical calculations show that the introduction of phosphorus vacancy moves the potential determining step of NO₃RR forward, which promotes the kinetic of the reaction. So, the conversion, Faraday efficiency and selectivity of catalyst are significantly improved. Furthermore, Zn-NO₃ battery exhibited power density of 1.05 mW cm⁻². This work has realized pollution treatment and energy conversion in electrocatalysis system and Zn-NO₃ battery system, enriched the application of vacancy engineering in this field.

1. Introduction

With the development of economy and society, the demand for ammonium fertilizer in industry and agriculture is increasing [1–3]. As an important chemical raw material, ammonia plays an irreplaceable role in the production of ammonium fertilizer [4–6]. At present, ammonia production still relies on the Haber-Bosch process developed in the last century using nitrogen and hydrogen at high temperature and pressure [7–9]. The production of ammonia is a great trial in terms of the storage of raw materials, the safety of transfer, and the harshness of the process [10,11]. In the continuous improvement of the method, the electrochemical technology is expected to be a very promising alternative method to convert nitrate into ammonium [12,13]. The strategy can not only eliminate nitrate pollution to water body, but also reduce energy demand without high energy consumption [14,15]. Until very recently, it has been found that the battery system for electrocatalytic conversion of nitrate to ammonium and Zn-NO₃ is actually a type of electrocatalytic system. If an efficient catalyst can be developed to apply both systems, it will be a kind of project with great theoretical and

application prospects [16–18].

NO₃⁻(aq) + 7H₂O + 8e⁻ → NH₄OH(aq) + 9OH⁻(aq), as the core reaction, plays an important role in the electrocatalytic nitrate reduction system and the Zn-NO₃ battery system [19]. To be specific, as a typical eight-electron nine-proton reaction, not only rapid electron transfer, but also accelerated kinetic process are needed to jointly enhance the intrinsic activity of electrocatalysts. On the one hand, in recent years, with the continuous development of electrocatalysis, heterogeneous interface engineering has become an important way to accelerate electron transfer and control electronic structure [20–22]. For example, through heterogeneous interface engineering, our research group [23] prepared Cu/Fe₂O₃ Schottky electrocatalysts, and enhanced the intrinsic NO₃-RR activity of electrocatalytic system by the directional flow of electrons at the heterogeneous interface between metallic Cu and semiconductor Fe₂O₃. On the other hand, vacancy engineering [24–27] and doping engineering [28,29] have also been introduced into the study of nitrate reduction to ammonium, which shows that it can promote the performance to some extent. For example, Chen [30] et al. successfully synthesized Cu₂O rich in oxygen vacancies, which

* Corresponding author.

E-mail address: huangfangzhi@163.com (F. Huang).

<https://doi.org/10.1016/j.apcatb.2023.122627>

Received 17 January 2023; Received in revised form 28 February 2023; Accepted 12 March 2023

Available online 14 March 2023

0926-3373/© 2023 Elsevier B.V. All rights reserved.

significantly improved performance by inhibiting HER reaction and promoting hydrogenation process kinetics. In addition to the application of the above engineering strategy in the electro catalytic nitrate reduction, researchers have also used doping engineering to realize the combined use of materials in electrocatalysis system and Zn-NO₃ battery system. For example, Sun et al. reported that iron doped Co₃O₄ nanoarrays realized the highly active ammonia production of NO₃RR by adjusting the important step of NO₃ adsorption [28]. More interestingly, Zhi [31] et al. prepared iron doped nickel phosphide (Fe/Ni₂P), which changed the electronic structure of the metal center by adjusting the downshift of the Ni₂P d-band center and promoting the strong interaction between Ni and Fe, thus affecting the electrocatalytic activity of Fe/Ni₂P. However, the research on the application of vacancy engineering in the electro catalytic system and Zn-NO₃ battery system has not been reported. Therefore, through the design of structural engineering and vacancy engineering, the development of a catalyst with unique nanostructure and rich active sites is still the breakthrough point of significant progress in electrocatalytic system and Zn-NO₃ battery system.

Meanwhile, as far as we know, one dimensional (1D) hollow nanotube has unique advantages in the field of electrocatalysis. When they are used as electrocatalysts, 1D hollow nanotubes have higher specific surface area and more active sites because their open front ends make them have both inner and outer surfaces [32]. As far as the active site is concerned, this is a very important factor, and various catalytic reactions, including the adsorption, conversion and desorption of substrates and intermediates, usually take place at the active site [33,34]. Secondly, due to the enhanced contact with electrolyte, 1D hollow nanotubes can promote the electron transport at the electrode/electrolyte interface, which is beneficial for multi-electron reaction [35]. Based on the above description, we have reason to believe that 1D hollow nanotube structure with high specific surface area and rapid interfacial electron transfer has great potential in the application of NO₃RR.

In view of all this, we report a one-dimensional nanotube array of heterogeneous bimetallic phosphide CoP-Ni₂P (label as CoNi-Vp-x) rich in phosphorus vacancies and its application in electrocatalytic NO₃RR system and Zn-NO₃ battery system. Benefiting from the high active area, rich phosphorus vacancy and superhydrophilicity, heterogeneous bimetallic phosphide CoP-Ni₂P nanotubes with the characteristics of promoting electron transfer exhibit excellent activity for electrocatalytic NO₃RR. Specifically, the introduction of phosphorus vacancy into the one-dimensional bimetallic hollow nanotube array can not only reduce the central energy level of the d-band, but also enhance the adsorption of NO₃, and can rarely realize the advance of the kinetic reaction decision step, and finally obtain excellent catalytic efficiency. The catalytic activity of CoNi-Vp-1.0 was significantly enhanced due to the control of phosphorus vacancy, specifically its Faraday efficiency of 84.27 % for NH₄⁺ synthesis and nearly 96 % NO₃ conversion with excited NH₄⁺ yield rate of 0.0977 mmol h⁻¹ cm⁻² at -0.9 V vs. RHE in 50 ppm NO₃-N + 0.5 M Na₂SO₄ aqueous solution. In addition, it was verified that Zn-NO₃ battery with Zn foil as anode and CoNi-Vp-1.0 as cathode has a good energy supply (1.05 mW cm⁻²) and simultaneously ammonium yield of 12.227 μmol h⁻¹ cm⁻² at 6 mA cm⁻² and Faradaic efficiency of 76.23 % at 4 mA cm⁻². The superior NO₃RR activity of CoNi-Vp originates from the fact that the phosphorus vacancy promotes the charge accumulation of Co, Ni and P atoms near the vacancy, and modulates the electronic configuration, so that the d-band center moves down from Fermi level. Meanwhile, the introduction of phosphorus vacancy makes the potential determination step move from *NO + H₂O + 2e⁻ → *N + 2OH⁻ to *NO₂ + H₂O + 2e⁻ → *NO + 2OH⁻ and the free energy of the potential determination step also decreases from 0.78 eV to 0.52 eV, which indicates that CoNi-Vp has more favorable NO₃RR kinetics than CoNi-P.

2. Experimental section

2.1. Chemical reagents

Ni foam (1 mm thickness) was purchased from Lizhiyuan battery sales department (Taiyuan, PR China). Cobalt nitrate hexahydrate (Co(NO₃)₂·6H₂O), Nickel nitrate hexahydrate (Ni(NO₃)₂·6H₂O), hydrochloric acid (HCl), acetone and ethanol were purchased from Sinopharm Chemical Reagent Co., Ltd. 2-methylimidazole (2-MIM) and polyvinylpyrrolidone (PVP) were purchased from Sigma-Aldrich. ammonium sulfate-¹⁴N ((¹⁴NH₄)₂SO₄, 98.5 %), ammonium sulfate-¹⁵N ((¹⁵NH₄)₂SO₄, ≥ 99 at. %, 98.5 %), sodium nitrate-¹⁴N (Na¹⁴NO₃, 98.5 %), sodium nitrate-¹⁵N (Na¹⁵NO₃, ¹⁵N ≥ 99 at. %, 98.5 %), Maleic acid (C₄H₄O₄, ≥ 99.0 %), Deuterium oxide (D₂O, 99 at. % D). Milli-Q water (18.25 MΩ cm⁻¹) was applied across the whole experiments.

2.2. Synthesis of materials

2.2.1. Preparation of ZIF-67

First, 0.05 M Co(NO₃)₂·0.6H₂O was mixed with 0.4 M 2-methylimidazole solution in equal volume. Then, the pre-treated NF was immersed in the above mixed solution and kept at room temperature for 4 h. Finally, rinse with deionized water (DIW) and ethanol for three times, and dry at 60 °C for standby.

2.2.2. Preparation of CoNi-LDH

The prepared ZIF-67 were immersed in 15 mL of 0.37 mM aqueous Ni(NO₃)₂·0.6H₂O solution, taken out after standing for 6 h at room temperature, washed with deionized water and ethanol, and dried at 60 °C.

2.2.3. Preparation of CoNi-Vp-x

Here, x represents the quality of phosphorus source. Detailed description in Table S1. First, CoNi-LDH were calcined at 400 °C for 2 h in a muffle furnace at a heating rate of 2 °C/min to get Cobalt nickel bimetallic oxide (CoNi-O). After that, phosphorus sources with different contents (0.2, 0.5 and 1.0 g NaH₂PO₂·H₂O) and CoNi-O were placed upstream and downstream of the quartz tube, respectively. Subsequently, the samples were calcined at 300 °C for 3 h under nitrogen atmosphere at a heating rate of 2 °C/min to obtain, CoNi-Vp-0.2, CoNi-Vp-0.5 and CoNi-Vp-1.0, respectively.

2.2.4. Preparation of CoNi-P-0.2

The preparation of CoNi-P-0.2 is basically the same as that of CoNi-Vp-0.2, except that it is phosphatized directly in nitrogen atmosphere by using CoNi-LDH.

3. Results and discussion

3.1. Characterization of materials

Heterogeneous bimetallic phosphide CoP-Ni₂P nanotube arrays with phosphorus vacancies (CoNi-Vp-x) was prepared by doping oxygen phosphating. Fig. 1a depicts the synthetic route of CoNi-Vp-x grown on foamed nickel. First, zeolitic imidazolate framework (ZIF-67) nanorod arrays with the uniform size were grown vertically on the foam nickel substrate (Fig. S1 and Fig. S2). Then, ZIF-67 nanorod arrays were used as the inner template, which was soaked in Ni²⁺ solution for a certain period of time, and it was transformed into CoNi-Layered Double Hydroxide (CoNi-LDH) nanotube arrays (Fig. S3). To be specific, during the formation of CoNi-LDH nanotube, protons produced by Ni²⁺ hydrolysis in the solution will gradually etch ZIF-67 nanorod, so that the coordinated Co²⁺ in ZIF-67 is released into the solution. At the same time, the released Co²⁺ and Ni²⁺ in the solution were coprecipitating to form a CoNi-LDH nanotube on the surface of ZIF-67 nanorod. With the extension of time, the internal template of ZIF-67 nanorod is consumed, and the CoNi-LDH nanotube are self-assembled to finally form graded

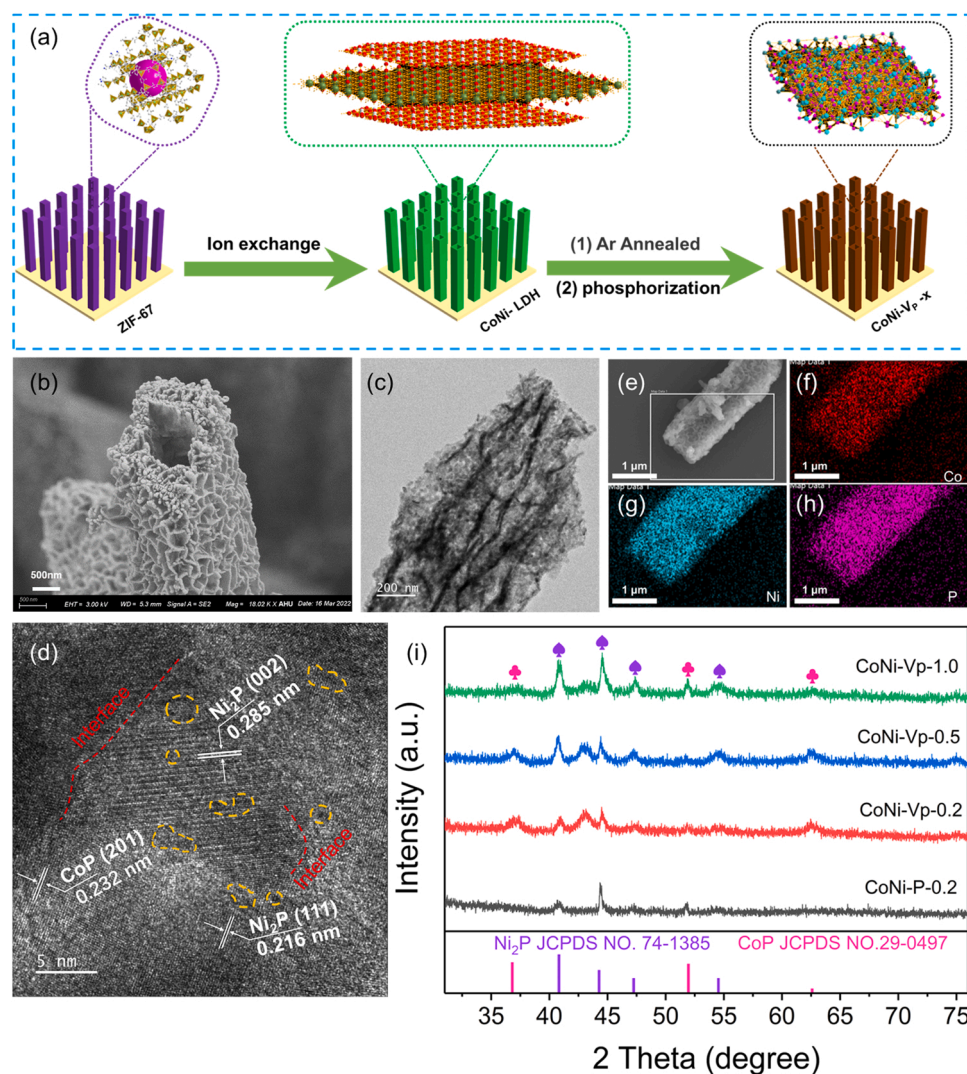


Fig. 1. (a) Schematic diagram of material synthesis. (b) SEM image of CoNi-Vp-1.0. (c) TEM images of CoNi-Vp-1.0. (d) HRTEM image of CoNi-Vp-1.0. (e-h) Elemental mapping images of Co, Ni, and P recorded from the same zone. (i) XRD patterns of CoNi-P-0.2, CoNi-Vp-0.2, CoNi-Vp-0.5 and CoNi-Vp-1.0, respectively.

hollow CoNi-LDH nanotube [36]. Since the metal center of ZIF-67 nanorod coordinates with the organic linker to form a special framework, the transformation from ZIF-67 nanorod to CoNi-LDH nanotube is very flexible. Furthermore, the dissociation and reconstruction process of the whole structure is orderly [37]. As shown in the energy dispersion spectrum (EDS) mapping displayed in Fig. S3d, all elements are evenly distributed in the structure. In the subsequent experiments, we successfully synthesized heterogeneous bimetallic phosphide CoP-Ni₂P with different phosphorus vacancy concentrations by doping oxygen induced strategy, which are labeled as CoNi-Vp-0.2, CoNi-Vp-0.5 and CoNi-Vp-1.0 nanotube, respectively [38]. It can be seen, with the increase of phosphorus source mass (0.2, 0.5, 1.0 g), the morphology of hollow nanotube is maintained and displayed in Fig. S4-S8. Meanwhile, the element percentages in CoNi-P-0.2, CoNi-Vp-0.2, CoNi-Vp-0.5 and CoNi-Vp-1.0 samples was also determined by ICP-AES and summarized in Table S2. Thereafter, as shown in the SEM and TEM diagrams in Fig. 1b and c, compared with CoNi-LDH nanotube and CoNi-O nanotube, the hollow tubular structure of CoNi-Vp-1.0 has no obvious change. However, after phosphating, the surface of the nanotubes became rough obviously. The high-resolution TEM diagram in Fig. 1d shows that the spacing between adjacent lattice fringes is 0.216, 0.285 and 0.232 nm, which is attributed to Ni₂P (111), Ni₂P (002) and CoP (201) planes, respectively [39–41]. It is worth noting that in Fig. 1d, the fracture and

discontinuity of lattice stripe can be clearly seen (indicated by yellow dotted line), which may be caused by phosphorus vacancy [42,43]. Subsequently, the corresponding element mapping of CoNi-Vp-1.0 shows the uniform distribution of Co, Ni and P species (Fig. 1e–h). In order to accurately analyze the phase of the sample, the X-ray diffraction spectra and Raman spectra of CoNi-P-0.2, CoNi-Vp-0.2, CoNi-Vp-0.5, CoNi-Vp-1.0 obtained by ultrasound from foam nickel were analyzed and shown in Fig. 1i and Fig. S9. As shown in Fig. 1i, the characteristic peaks of all samples are well matched with Ni₂P (JCPDS No. 74–1385) and CoP (JCPDS No. 29–0497) [44,45]. The Raman peaks at 680 cm^{−1} further confirm the crystal structure of CoP in CoNi-P-0.2, CoNi-Vp-0.2, CoNi-Vp-0.5, CoNi-Vp-1.0 (Fig. S9) [46]. It is worth noting that Ni₂P has no obvious Raman characteristic peak, which is consistent with the previous results on Ni₂P [47,48]. In addition, the absence of oxides in the sample was further confirmed by XRD and locally amplified Raman spectroscopy (Fig. S10). Specifically, at 446 cm^{−1}, 530 cm^{−1} and 585 cm^{−1}, 704 cm^{−1}, there are no characteristic Raman peaks representing Ni–O and Co–O bonds, respectively, which further indicates that there are no partial oxides in the sample. The above results show that CoNi-Vp-x with high uniformity in shape and size have been successfully prepared by the proposed method.

The high-resolution XPS spectra further revealed the structural differences between CoNi-P-0.2 and CoNi-Vp-x with different phosphorus

vacancy concentrations to deepen the understanding of electronic interaction. The XPS survey spectrum of the as-synthesized CoNi-P-0.2 and CoNi-Vp-x in Fig. 2a indicates the obvious existence of Co, Ni, P, C and O elements. As shown in Fig. 2b, the high-resolution Co 2p spectrum is deconvoluted into three peaks centered on 777.65 (Co-P), 781.6 (Co-O) and 786.15eV (satellite peak) [41,49]. Importantly, the Co-P peak of CoNi-Vp-x shifts to a lower binding energy as compared to that of CoNi-P-0.2, indicating the formation of phosphorus vacancy [50]. Similarly, in the high-resolution Ni 2p spectrum of Fig. 2c, the obvious peaks at 876.70 and 870.35 eV are attributed to the satellite peaks formed by spin-orbit splitting of Ni 2p_{1/2}, the peak at 858.23eV is related to the Ni-O species formed by surface oxidation, and the peak at 852.89eV indicates the formation of Ni-P bonds [51]. In addition, by comparison, the Ni-P peak in CoNi-Vp-x also moved to the direction of lower binding energy, again indicating the formation of phosphorus vacancy [52]. As exhibited in Fig. 2d, the P 2p spectrum shows four peaks at 134.11, 133.26, 130.26 and 129.21 eV. The first two distinct peaks at 134.11 and 133.26 eV were designated as surface P-O species due to the exposure in the air. The other two peaks at 130.26 and 129.21 eV can be associated with the P-Ni and P-Co species in CoNi-Vp-1.0, which consistent well with the 777.7 eV in Co 2p and 852.6 eV in Ni 2p, respectively [53,54]. Compared with CoNi-P-0.2, CoNi-Vp-0.2 and CoNi-Vp-0.5, the peak of CoNi-Vp-1.0 (P-Ni peak of

P 2p_{1/2} and P-Co peak of P 2p_{3/2}) have the lower binding energy, revealing the existence of phosphorus vacancy and the increasing trend of its concentration in the sample [55]. The peak centers corresponding to the characteristic peaks of each sample are clearly shown in Fig. 2e. It can be found that compared with CoNi-P-0.2, CoNi-Vp-0.2 and CoNi-Vp-0.5, the peaks of CoNi-Vp-1.0 (Co-P peak in Co 2p, Ni-P peak in Ni 2p, P-Co and P-Ni peaks in P 2p) have the lowest binding energy, which indicates that more electrons are accumulated on Co, Ni and P with the increase of phosphorus vacancy concentration [56]. In other words, due to the existence of phosphorus vacancy, there is a trend of electron enrichment on Co, Ni and P atoms [57]. Electron paramagnetic resonance (EPR) measurement further qualitatively confirmed the existence of phosphorus vacancy with different concentrations. As shown in Fig. 2f, CoNi-P-0.2 does not show significant EPR signal, while CoNi-Vp-0.2, CoNi-Vp-0.5 and CoNi-Vp-1.0 showed remarkable signal at g-value of 2.002, which was derived from unpaired electrons captured by surface phosphorus vacancy [51]. Meanwhile, compared with CoNi-Vp-0.2 and CoNi-Vp-0.5, CoNi-Vp-1.0 showed stronger EPR signal, which confirmed the existence of higher concentration phosphorus vacancy. It is reported that the hydrophilicity of materials is very important to the catalytic process, and vacancy have unique advantages in regulating hydrophilicity [58]. Therefore, we measured the contact angle of electrolyte solution on the surface of materials, on the one hand,

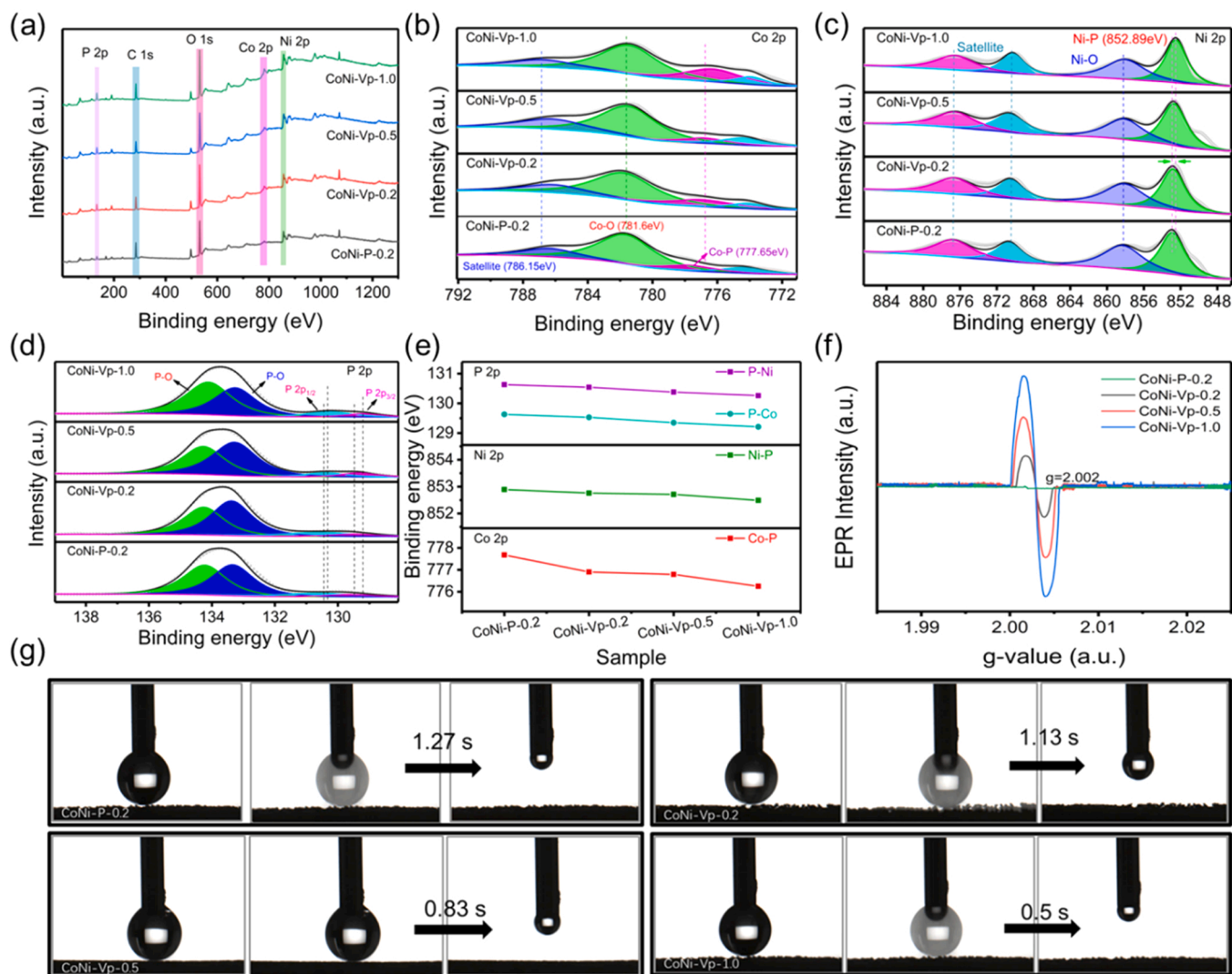


Fig. 2. (a) XPS all spectra, (b) High-resolution XPS spectra of Co 2p, (c) High-resolution XPS spectra of Ni 2p, (d) High-resolution XPS spectra of P 2p, (e) The binding energy corresponding to each standard diffraction peak. (f) EPR spectra (g) Electrolyte contact angle of CoNi-P-0.2, CoNi-Vp-0.2, CoNi-Vp-0.5 and CoNi-Vp-1.0.

to determine the hydrophilic property of materials surface, and on the other hand, to evaluate the content of vacancy on the surface of materials through the diffusion and absorption time of electrolyte solution on the materials surface [59]. Firstly, the hydrophilicity of CoNi-P-0.2, CoNi-Vp-0.2, CoNi-Vp-0.5 and CoNi-Vp-1.0 was estimated by the contact angle of electrolyte solution (0.5 M Na₂SO₄), as shown in Fig. 2g. It can be seen, when the materials contacts with 0.5 M Na₂SO₄ electrolyte in the air, the droplets rapidly diffuse and absorb when the contact angle is 0°, indicating the materials has excellent hydrophilicity. In fact, hydrophilic surface is very desirable because it can promote the initial adsorption of reactants on the electrode surface, which is conducive to the overall kinetics of electrocatalytic nitrate reduction [60]. Secondly, by observing the penetration time of electrolyte on CoNi-P-0.2, CoNi-Vp-0.2, CoNi-Vp-0.5 and CoNi-Vp-1.0, we found that the penetration time changed from the initial 1.27–0.5 s, which confirmed the increasing trend of phosphorus vacancy concentration. Through the above tests, we have qualitatively determined the phosphorus vacancy concentration in CoNi-P-0.2, CoNi-Vp-0.2, CoNi-Vp-0.5 and CoNi-Vp-1.0.

3.2. Electrocatalytic NO₃RR activity

To study the effect of phosphorus vacancy concentration on

electrocatalytic activity, a single chamber electrolyze was used to evaluate the NO₃RR activity of the catalyst. All potentials in this work are based on RHE scale. Meanwhile, NO₃RR products including NO₃⁻, NO₂⁻, NH₄⁺ were quantified by colorimetry methods as shown in Fig. S11 [61]. By comparing the current responses of different samples in electrolyte solution, the activity of NO₃RR was qualitatively evaluated. Fig. 3a shows the linear sweep voltammograms (LSV) curves of CoNi-P-0.2, CoNi-Vp-0.2, CoNi-Vp-0.5, and CoNi-Vp-1.0 in 0.5 M Na₂SO₄ with and without 50 ppm NO₃-N. It shows a tight reduction current in 0.5 M Na₂SO₄ solution without 50 ppm NO₃-N, which is usually attributed to hydrogen evolution reaction (HER) [62]. It is worth noting that the reduction current of each catalyst electrode in 0.5 M Na₂SO₄ solution containing 50 ppm NO₃-N is much greater than that in 0.5 M Na₂SO₄ solution without 50 ppm NO₃-N. Furthermore, with the increase of phosphorus vacancy concentration, the value of reduction current also shows an increasing trend, which indicates that the increase of phosphorus vacancy concentration has a positive effect on the activity of NO₃RR [63]. To study the activity and selectivity of each catalyst for NO₃RR in more detail, the concentration of NO₃⁻-N, NO₂⁻-N, NH₄⁺-N in the solution was quantitatively analyzed by colorimetry methods and displayed in Fig. S12. The CoNi-P-0.2, CoNi-Vp-0.2, CoNi-Vp-0.5, and CoNi-Vp-1.0 show gradually increasing nitrate conversion and volcanic Faraday efficiency, selectivity, ammonium yield rate with the more

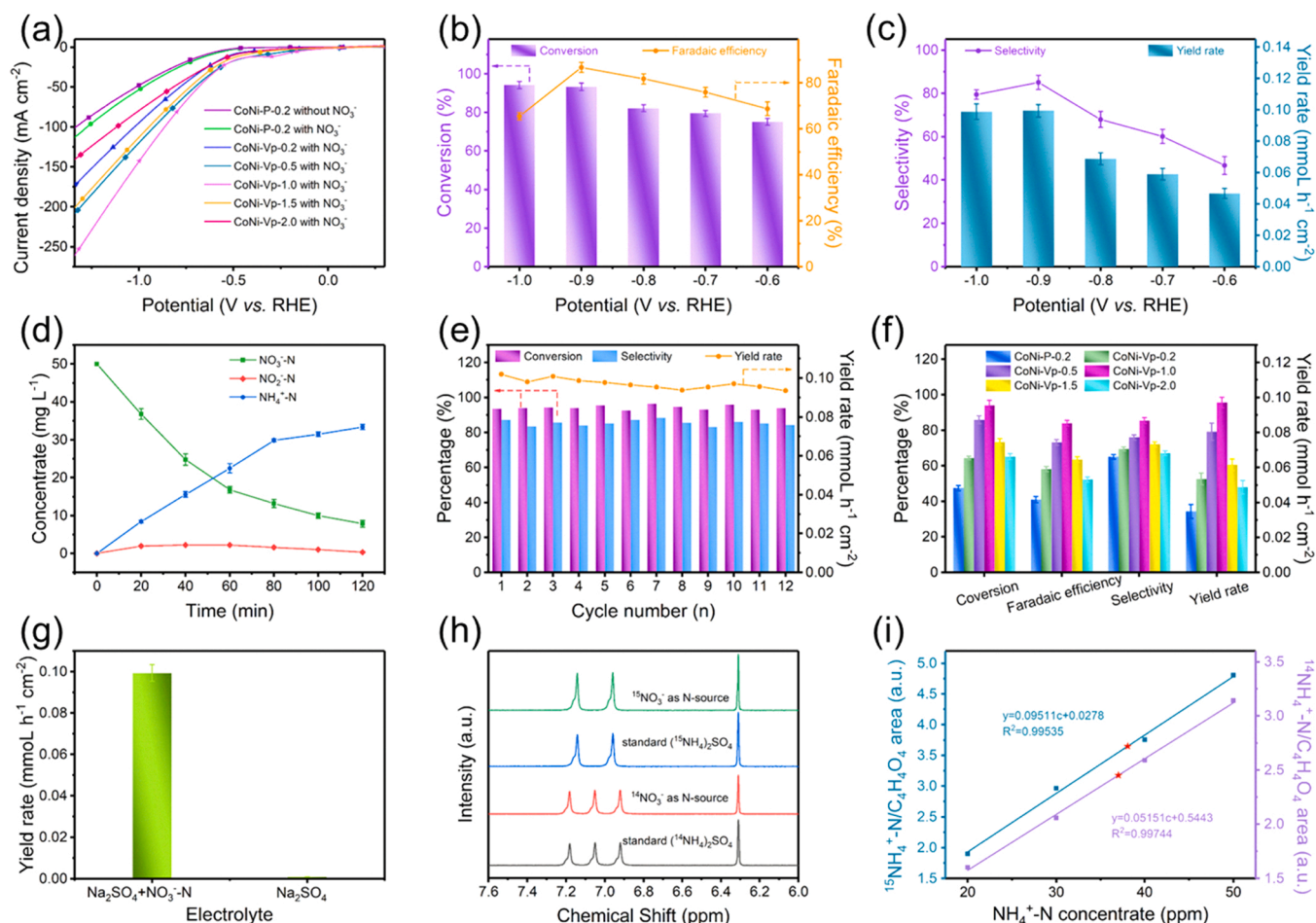


Fig. 3. (a) LSV curves of CoNi-P-0.2, CoNi-Vp-0.2, CoNi-Vp-0.5 and CoNi-Vp-1.0 in 0.5 M Na₂SO₄ and 0.2 M Na₂SO₄ + 50 ppm NO₃-N electrolytes. (b) The conversion rate of nitrates and the Faradaic efficiency of ammonium over CoNi-Vp-1.0 electrocatalysts. (c) The selectivity and yield rate of ammonium over CoNi-Vp-1.0 electrocatalysts. (d) Time-dependent concentrations of NO₃⁻, NO₂⁻, and NH₄⁺ over CoNi-Vp-1.0 electrocatalysts at -0.9 V vs. RHE. (e) Consecutive recycling test at -0.9 V vs. RHE for CoNi-Vp-1.0. (f) The conversion rates of nitrates and the Faradaic efficiency, selectivity, and yield rate of ammonium over different samples. (g) Ammonium yield rate over CoNi-Vp-1.0 in Na₂SO₄ electrolyte with and without nitrate. (h) ¹H NMR spectra (600 MHz) of standard samples [(¹⁵NH₄)₂SO₄ and (¹⁴NH₄)₂SO₄] and electrolyte after the NO₃⁻ reduction at -0.9 V vs. RHE for 2 h using ¹⁴NO₃⁻ and ¹⁵NO₃⁻ as N-source. (i) The standard curve of integral area (NH₄⁺-N/C₄H₄O₄) against NH₄⁺-N concentration.

negative potentials while CoNi-Vp-1.0 show larger nitrate conversion, Faraday efficiency, selectivity, and ammonium yield rate compared to CoNi-P-0.2, CoNi-Vp-0.2, CoNi-Vp-0.5 at each given potential. Meanwhile, the selectivity of each sample to nitrite and ammonium is shown in Fig. S13 and S14. It can be found that the selectivity of nitrite gradually decreases with the potential becomes negative, and CoNi-Vp-1.0 has the best ammonium selectivity at each given potential. Based on the best NO₃RR activity shown by CoNi-Vp-1.0, it was selected as an ideal catalyst to study the activity of NO₃RR. In addition to studying the effect of phosphorus vacancy concentration on performance, we also synthesized CoP and CoP-Ni₂P without phosphorus vacancy (CoNi-P-0.2) sample to study the enhancement effect of heterogeneous bimetallic phosphide. As shown in Fig. S15, at the same potential, compared with CoP and CoP-Ni₂P has better catalytic performance, which further reflects the improvement effect of performance by heterogeneous bimetallic phosphide. Through the above research, we further confirmed that the improvement of NO₃RR performance is achieved through the synergistic modulation of phosphorus vacancy and heterogeneous bimetallic phosphide CoP-Ni₂P.

In light of these evidences, we performed a series of electrochemical experiments to investigate the electrocatalytic NO₃RR performance of CoNi-Vp-1.0 in detail. As shown in Fig. 3b, c, from -0.6 V to -1.0 V vs. RHE, the conversion of nitrate gradually increased while the Faradaic efficiency, selectivity and ammonium yield rate showed a volcano shape curve with a maximum 84.27 %, 85.23 % and 0.0977 mmol h⁻¹ cm⁻² at -0.9 V vs. RHE, respectively. Therefore, we choose -0.9 V vs. RHE as the operation voltage. Fig. 3d shows the curve of the concentration of NO₃-N, NO₂-N, NH₄⁺-N with time under the potential of -0.9 V vs. RHE. With the extension of reaction time, the concentration of nitrate decreases gradually and the concentration of ammonium increases while the concentration of nitrite increases first and then decreases, which means that CoNi-Vp-1.0 has high selectivity for NH₄⁺, and match the data results in Fig. S16. The excellent catalytic activity of CoNi-Vp-1.0 was further verified by evaluating the electrochemical active area of the sample (Fig. S17). The nitrate conversion, ammonium selectivity, and yield rate shown in Fig. 3e did not show significant decay after twelve cycles. When the concentration of NO₃-N increased from 30 to 100 ppm, the conversion, Faraday efficiency, selectivity and ammonium yield rate showed acceptable changes, further revealing the wide application range of the catalyst. In addition, when the supporting electrolyte is changed to PBS solution (pH=7), the performance of the catalyst is basically maintained (Fig. S18). In addition, the SEM patterns of the materials after the electrocatalytic NO₃RR test also showed no significant changes (Fig. S19). The XRD pattern of the catalyst and the concentration of Co²⁺ and Ni²⁺ in the electrolyte after cyclic electrolysis further highlight the excellent durability of the catalyst (Fig. S20). Meanwhile, the XPS measurement results of the samples of CoNi-P-0.2, CoNi-Vp-0.2, CoNi-Vp-0.5, and CoNi-Vp-1.0 after the electrocatalytic NO₃RR test in Fig. S21 also proved the structural robustness. And the NO₃RR performance of CoNi-P-0.2, CoNi-Vp-0.2, CoNi-Vp-0.5, and CoNi-Vp-1.0 at -0.9 V vs. RHE was studied and compared in Fig. 3f. The nitrate conversion rate, Faradaic efficiency, ammonium selectivity, and yield rate of CoNi-Vp-1.0 was 95.46 %, 84.27 %, 85.23 % and 0.0977 mmol h⁻¹ cm⁻², respectively, obviously higher than those of CoNi-Vp-0.5 (88.40 %, 71.45 %, 76.32 %, 0.0811 mmol h⁻¹ cm⁻²), CoNi-Vp-0.2 (64.79 %, 59.83 %, 69.38 %, 0.0561 mmol h⁻¹ cm⁻²) and CoNi-P-0.2 (47.66 %, 41.08 %, 66.23 %, 0.0394 mmol h⁻¹ cm⁻²). The excellent potential of CoNi-Vp-1.0 on NO₃RR is further demonstrated by the above performance evaluation.

To verify the ammonium produced in the experiment really comes from electrocatalysis of NO₃RR, we conducted a blank control experiment. The electrolysis of the blank Na₂SO₄ solution produced almost negligible ammonium, whereas the Na₂SO₄/NO₃ solution produced significant ammonium production, as shown in Fig. 3g. Meanwhile, ¹⁴NO₃-N and ¹⁵NO₃-N were used as nitrogen sources for isotope labeling experiments [64]. The nuclear magnetic resonance spectrum of

¹⁴NH₄⁺-N and ¹⁵NH₄⁺-N in the solution after electrolysis shows triple peaks and double peaks, respectively, which is consistent with the standard ¹⁴NH₄⁺-N and ¹⁵NH₄⁺-N, further confirming that ammonium comes from electrocatalytic NO₃RR (Fig. 3h, and Fig. S22 and S23). In addition, the ammonium produced was quantified by nuclear magnetic resonance. The results show that the quantitative results of generated ammonium are almost close to those determined by UV-vis spectrophotometry, which confirms the accuracy of the quantitative method of ammonium (Fig. 3i and Table S3).

3.3. Zn-NO₃ battery activity

After confirming the excellent NO₃RR activity of CoNi-Vp-1.0, we further assembled a novel Zn-NO₃ battery with CoNi-Vp-1.0 as cathode and Zn foil as anode. As shown in Fig. 4a, a typical H-type electrolytic cell separated by a proton exchange membrane contains 30 mL cathode electrolyte (0.5 M Na₂SO₄ + 5 mM NaNO₃-N) and 30 mL anode electrolyte (1 M KOH). Fig. 4b shows that CoNi-Vp-1.0 based battery exhibits a constant open circuit voltage of 1.03 V vs. Zn/Zn²⁺. Although the voltage is lower than 1.87 V vs. Zn/Zn²⁺ theoretical value due to relatively large cathodic polarization caused by excellent chemical stability and complex reaction path, its performance can still be expected as an emerging field. Fig. 4c shows the discharge LSV curve of CoNi-Vp-1.0 based battery. It can be found that the output current density increases with the cathode potential becomes negative, and the maximum power density of the battery reaches 1.05 mW cm⁻². Interestingly, as a new type of primary battery developed, it can supply power for electronic timers for more than 90 min, which verifies the feasibility from the perspective of application (Fig. 4d). In addition, the discharge curves of the CoNi-Vp-1.0 based battery at different current densities from 0.05 to 6 mA cm⁻² are shown in Fig. 4e. The output voltage can always be kept relatively constant at the initial 0.05 mA cm⁻² and keep 1 h, and the output voltage at other current density is also basically maintained, further demonstrating its remarkable stability. Meanwhile, the charge-discharge curves of the Zn-NO₃ battery that shown in Fig. S24 at different current density also demonstrate its outstanding stability. It is worth noting that the Zn-NO₃ battery system is a system that kills two birds with one stone, specifically, self-driving the synthesis of ammonium utilizing the electricity generated by the battery itself. The electrochemical performance of the Zn-NO₃ battery system has been evaluated previously, and the synthesis of self-driven ammonium will be explored next. The ammonium yield rate and Faradaic efficiency when discharged for 2 h at different current density are shown in Fig. 4f. We were surprised to find that the CoNi-Vp-1.0 based cell achieved an ammonium yield rate of 12.227 μmol h⁻¹ cm⁻² at 6 mA cm⁻² and a high Faradaic efficiency of 76.23 % at 4 mA cm⁻². In addition, the long-term test in Fig. 4g shows that under the fixed current density of 4 mA cm⁻², the ammonium yield rate and Faraday efficiency deviate slightly but are basically stable, indicating the long-term stability of Zn-NO₃ battery in ammonium synthesis. Notably, CoNi-Vp-1.0 exhibited outstanding performance in both electrocatalytic and battery systems compared with other reported studies (Fig. 4h, Table S4 and S5). In addition, we also compared the performance of the CoNi-Vp-1.0 catalyst with that of the Zn-air battery reported in the literature, and showed the detailed results in Table S6.

3.4. Elucidation of the NO₃RR mechanism

In order to further explore the mechanism of improving electrochemical performance by phosphorus vacancy, density functional theory (DFT) calculations were carried out. According to the XRD, HRTEM pattern and microstructure analysis, CoP (201) and Ni₂P (111) crystal plane in heterogeneous bimetallic phosphide CoNi-P and CoNi-Vp were selected as exposure site. First, the optimized CoNi-P and CoNi-Vp model maps were drawn to study the differences in electronic configurations (Fig. 5a and b). Fig. 5c and d show 3D electron localization function

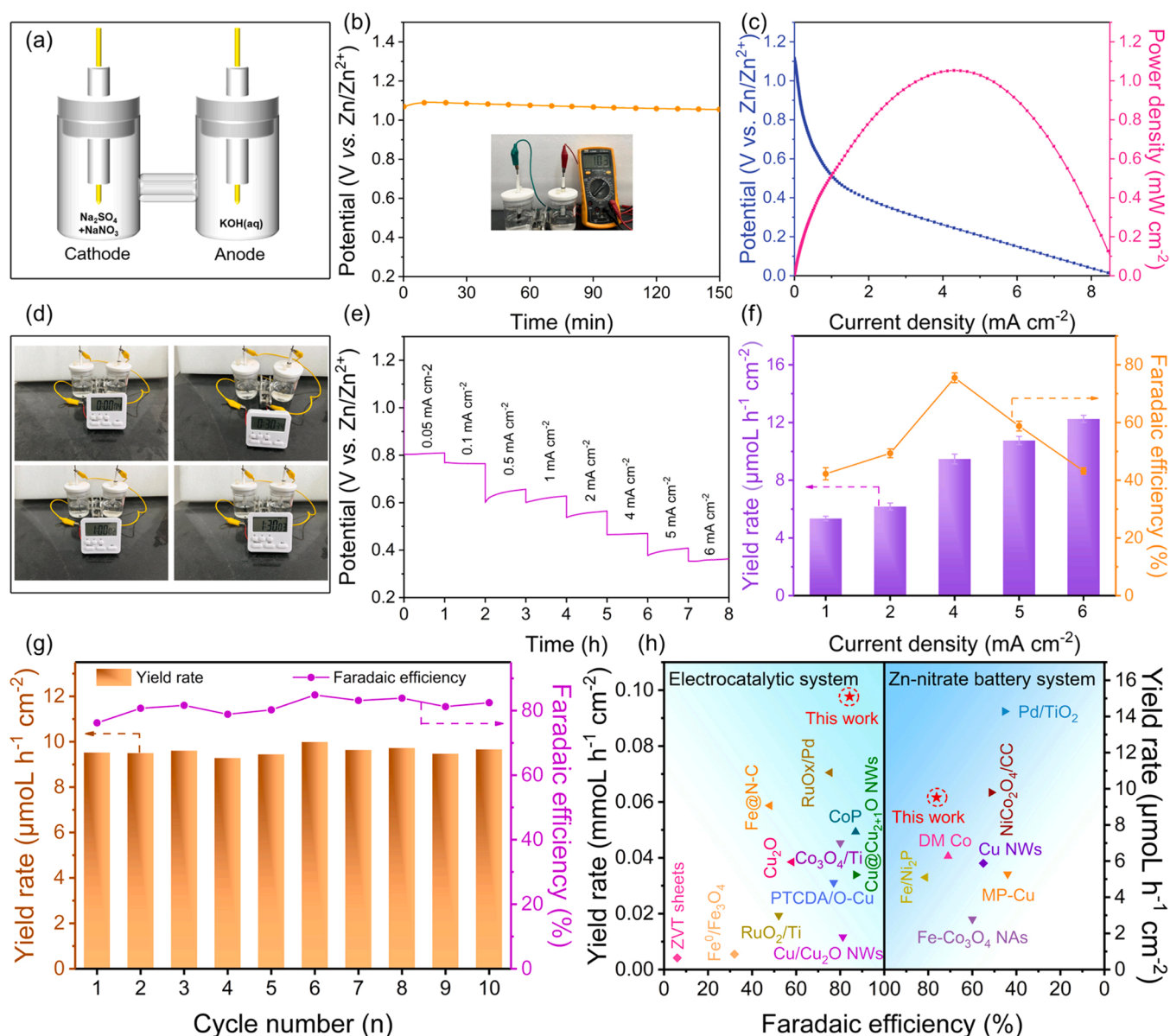


Fig. 4. (a) The concept diagram of Zn-NO₃ battery. (b) Open circuit voltage of CoNi-Vp-1.0 based Zn-NO₃ battery. (c) Discharging curves and the resultant power density curve of the CoNi-Vp-1.0 based Zn-NO₃ battery. (d) Demonstration experiment of Zn-NO₃ battery supplying power for electronic timer. (e) Discharging curves at different current densities. (f) Faradaic efficiency and NH₄⁺ yield rate of Zn-NO₃ battery with CoNi-Vp-1.0 catalyst cathode at different current densities. (g) The long-term stability experiment of Zn-NO₃ battery at 4 mA cm⁻². (h) Faraday efficiency and ammonium yield rate of CoNi-Vp-1.0 are compared with reported electrocatalytic NO₃RR and Zn-NO₃ based catalysts.

diagrams of the above two materials, wherein the green region and the blue region represent charge accumulation and depletion, respectively. At the same time, the 3D Bader charge diagram (Fig. 5e and f) clearly shows that the number of electrons lost by Co and Ni atoms is significantly reduced after the introduction of phosphorus vacancy, which means that the introduction of phosphorus vacancy is conducive to the accumulation of electrons at Co and Ni sites, which is consistent with the XPS results. Here, positive and negative values in the 3D Bader charge diagram represent the accumulation and depletion of electrons, respectively. The difference of electronic configuration between CoNi-P and CoNi-Vp can also be shown by the density of states (DOS). As shown in Fig. 5g and h, compared with CoNi-P (−1.389 eV), the d-band center of CoNi-Vp (−1.397 eV) downshifts towards Fermi level, which is consistent with the result of the negative shift of the binding energy of Co 2p, Ni 2p and P 2p in XPS. According to the d-band center theory, the energy level of the d-band center decreases, and the adsorption capacity

of its surface with NO₃RR intermediate decreases [65]. Therefore, the introduction of phosphorus vacancy will adjust the electronic structure of CoNi-Vp, optimize the adsorption of intermediates, and then affect the catalytic activity.

In addition, we analyzed the preferential adsorption of NO₃ on CoNi-P and CoNi-Vp. The structure optimized CoNi-P and CoNi-Vp models after adsorbing NO₃ are shown in Fig. S25, and the adsorption energy of NO₃ is calculated. As we all know, in NO₃RR, the first and most important step is the adsorption of nitrate, that is, the process of nitrate from free state in solution to adsorbed state. The optimal adsorption of nitrate is critical, which will inhibit the competitive adsorption of other anions in the solution and promote the overall NO₃ reduction reaction under the action of proton-electron pairs. As shown in Fig. 5i, the adsorption energy of −3.72 eV of NO₃ on CoNi-Vp is more negative (−3.39 eV) than that of CoNi-P. The more negative the adsorption energy, the stronger the adsorption of NO₃. Therefore, NO₃ showed a

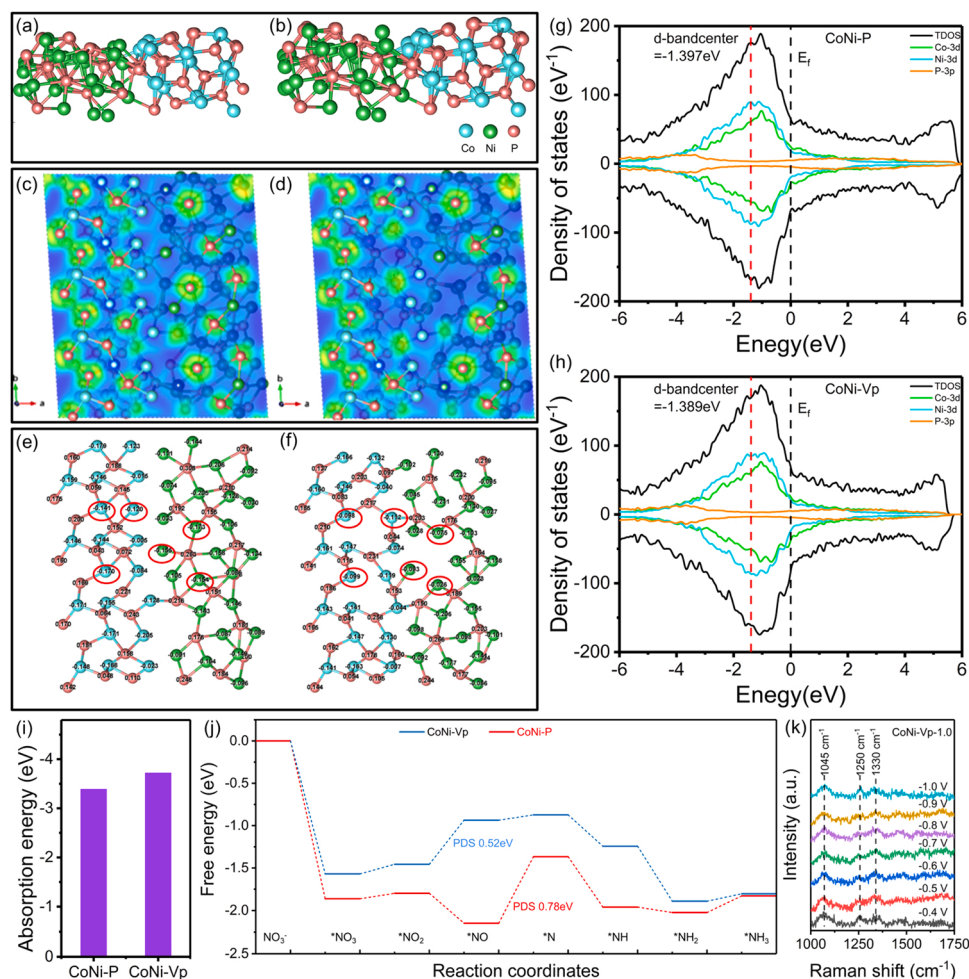


Fig. 5. The schematic diagram of atomic structure of (a) CoNi-P and (b) CoNi-Vp. The 3D electronic localization function diagrams of (c) CoNi-P and (d) CoNi-Vp. The 3D Bader charge diagram of (e) CoNi-P and (f) CoNi-Vp. The DOS diagram of (g) CoNi-P and (h) CoNi-Vp. (i) The adsorbing energy of NO_3^- on CoNi-P and CoNi-Vp. (j) The calculated adsorption free energies on CoNi-P and CoNi-Vp toward different N-containing intermediates. (k) In-situ Raman Spectra of CoNi-Vp-1.0.

stronger adsorption strength in CoNi-Vp, which was conducive to promoting the subsequent NO_3RR .

Subsequently, we calculated the free energies of different adsorption intermediates on the surfaces of CoNi-P and CoNi-Vp. According to the literature, NO_3RR ($\text{NO}_3^- + 7\text{H}_2\text{O} + 8\text{e}^- = \text{NH}_4\text{OH} + 9\text{OH}^-$) includes a series of deoxygenation reactions and hydrogenation reactions. In order to study the potential mechanism of the NO_3RR pathway, we performed density functional theory calculations and used the most stable adsorption model to retrieve the free energies of different reaction intermediates on the two catalyst models (Fig. S26, S27). The free energy of the NO_3RR reaction path in Fig. 5j shows that the free energy of the reaction intermediates of CoNi-Vp is also higher than that of CoNi-P and closer to zero. This result indicates that the introduction of phosphorus vacancy accelerates the kinetics of NO_3RR . In addition, more detailed data show that the introduction of phosphorus vacancy makes the potential determination step move from $^*\text{NO} + \text{H}_2\text{O} + 2\text{e}^- \rightarrow ^*\text{N} + 2\text{OH}^-$ to $^*\text{NO}_2 + \text{H}_2\text{O} + 2\text{e}^- \rightarrow ^*\text{NO} + 2\text{OH}^-$ and the free energy of the potential determination step also decreases from 0.78 eV to 0.52 eV, which indicates that CoNi-Vp has more favorable NO_3RR kinetics than CoNi-P. Next, we measured in-situ Raman spectroscopy to verify the effect of phosphorus vacancy introduction on kinetics by changing the proportion of NO_2^- intermediates. As shown in Fig. 5k and S24, it can be seen that the characteristic peaks at 1045 cm^{-1} , 1250 cm^{-1} and 1330 cm^{-1} of the Raman spectra of CoNi-Vp-1.0 and CoNi-P-0.2 are attributed to the tensile vibration of NO_3^- , $\text{N}=\text{O}$ between metal and nitrite and the adsorption of ammonia, respectively [66]. At the same time, as shown in

Fig. S28, S29, under the same potential, compared with CoNi-P-0.2, CoNi-Vp-1.0 has a lower proportion of NO_2^- intermediates in the electrocatalytic reduction process, which further verifies that the introduction of phosphorus vacancy can improve the overall dynamics. In general, the results of the above theoretical calculations and in-situ Raman provide theoretical support for the introduction of phosphorus vacancy to improve the catalytic performance. Therefore, it is chosen to be an ideal catalyst for further characterize and study the NO_3RR activity.

4. Conclusion

In summary, we successfully synthesized 1D heterogeneous bimetallic phosphide $\text{CoP-Ni}_2\text{P}$ nanotubes with different phosphorus vacancy concentrations, and discussed the effect of phosphorus vacancy concentration on the electrocatalytic performance. The results of experiment and theoretical calculation show that the electronic structure of CoNi-Vp is obviously adjusted after the introduction of phosphorus vacancy, which makes the electrons on the atoms near the vacancy accumulate. Meanwhile, the d-band center in CoNi-Vp downshift to the Fermi level, which optimizes the adsorption of intermediates and further improves the catalytic performance. By engineering phosphorus vacancy, CoNi-Vp-1.0 exhibited an impressive NH_4^+ yield of $0.0977\text{ mmol h}^{-1}\text{ cm}^{-2}$ and Faraday efficiency of 84.27 % at -0.9 V vs. RHE, with the 95.46 % conversion. In addition, we developed a novel Zn-NO_3^- battery by integrating NO_3RR electrocatalyst with Zn foil. The

battery has a power density of 1.05 mW cm^{-2} and a Faraday efficiency of 76.23 % for NH_4^+ production, which is superior to most of the reported Zn- NO_3 battery systems in terms of NH_4^+ yield and efficiency.

CRedit authorship contribution statement

Yihong Gao: Conceptualization, Investigation, Formal analysis, Data curation, Methodology, Writing-original draft, Writing-review & editing. **Kunpeng Wang:** Conceptualization, Investigation, Formal analysis, Data curation, Validation. **Chao Xu:** Formal analysis, Data curation, theoretical calculation. **Hao Fang:** Investigation, Formal analysis, Data curation. **Huili Yu:** Conceptualization, Data curation. **Hui Zhang:** Methodology, Investigation. **Shikuo Li:** Methodology, Investigation. **Chuanhao Li:** Formal analysis, Performed the theoretical calculations. **Fangzhi Huang:** Conceptualization, Data curation, Formal analysis, Funding acquisition, Resources, Supervision.

Declaration of Competing Interest

The authors declare that they have no known competing financial interests or personal relationships that could have appeared to influence the work reported in this paper.

Data Availability

Data will be made available on request.

Acknowledgements

This work is supported by the National Natural Science Foundation of China (Grant Nos. 52172174, 51872002, and 21771001), Science and Technology Planning Project of Guangdong Province (2020A0505100032), the Key Research and Development Projects in Anhui Province (202004a07020026), the Program of Anhui Scientific and Technical Leaders Reserve Candidates (2018RH168).

Appendix A. Supporting information

Supplementary data associated with this article can be found in the online version at [doi:10.1016/j.apcatb.2023.122627](https://doi.org/10.1016/j.apcatb.2023.122627).

References

- [1] M. Xia, C. Mao, A. Gu, A.A. Tountas, C. Qiu, T.E. Wood, Y.F. Li, U. Ulmer, Y. Xu, C. J. Viasus, J. Ye, C. Qian, G. Ozin, Solar urea: towards a sustainable fertilizer industry, *Angew. Chem. Int. Ed.* 61 (2022), e202110158.
- [2] L. Kekedy-Nagy, M. Abolhassani, S.I. Perez Bakovic, Z. Anari, J.P. Moore, Ii, B. G. Pollet, L.F. Greenlee, Electroless production of fertilizer (struvite) and hydrogen from synthetic agricultural wastewaters, *J. Am. Chem. Soc.* 142 (2020) 18844–18858.
- [3] N. López-Vinent, A. Cruz-Alcalde, J. Giménez, S. Esplugas, C. Sans, Improvement of the photo-fenton process at natural condition of pH using organic fertilizers mixtures: Potential application to agricultural reuse of wastewater, *Appl. Catal. B Environ.* 290 (2021), 120066.
- [4] G. Akay, Sustainable ammonia and advanced symbiotic fertilizer production using catalytic multi-reaction-zone reactors with nonthermal plasma and simultaneous reactive separation, *ACS Sustain. Chem. Eng.* 5 (2017) 11588–11606.
- [5] M.A. Legare, G. Belanger-Chabot, M. Rang, R.D. Dewhurst, I. Krummenacher, R. Bertermann, H. Braunschweig, One-pot, room-temperature conversion of dinitrogen to ammonium chloride at a main-group element, *Nat. Chem.* 12 (2020) 1076–1080.
- [6] M. Ali, F. Zhou, K. Chen, C. Kotzur, C. Xiao, L. Bourgeois, X. Zhang, D. R. MacFarlane, Nanostructured photoelectrochemical solar cell for nitrogen reduction using plasmon-enhanced black silicon, *Nat. Commun.* 7 (2016) 11335.
- [7] P.H. Langevelde, I. Katsounaros, M.T.M. Koper, Electrocatalytic nitrate reduction for sustainable ammonia production, *Joule* 5 (2021) 290–294.
- [8] G.-F. Chen, Y. Yuan, H. Jiang, S.-Y. Ren, L.-X. Ding, L. Ma, T. Wu, J. Lu, H. Wang, Electrochemical reduction of nitrate to ammonia via direct eight-electron transfer using a copper-molecular solid catalyst, *Nat. Energy* 5 (2020) 605–613.
- [9] S. Licht, B. Cui, B. Wang, F.-F. Li, J. Lau, S. Liu, Ammonia synthesis by N_2 and steam electrolysis in molten hydroxide suspensions of nanoscale Fe_2O_3 , *Science* 345 (2014) 637–640.
- [10] J.G. Chen, R.M. Crooks, L.C. Seefeldt, K.L. Bren, R.M. Bullock, M.Y. Darensbourg, P.L. Holland, B. Hoffman, M.J. Janik, A.K. Jones, M.G. Kanatzidis, P. King, K. M. Lancaster, S.V. Lyman, P. Pfromm, W.F. Schneider, R.R. Schrock, Beyond fossil fuel-driven nitrogen transformations, *Science* 360 (2018) 873–879.
- [11] B.M. Comer, P. Fuentes, C.O. Dimkpa, Y.-H. Liu, C.A. Fernandez, P. Arora, M. Realf, U. Singh, M.C. Hatzell, A.J. Medford, Prospects and challenges for solar fertilizers, *Joule* 3 (2019) 1578–1605.
- [12] Y. Zhao, Y. Liu, Z. Zhang, Z. Mo, C. Wang, S. Gao, Flower-like open-structured polycrystalline copper with synergistic multi-crystal plane for efficient electrocatalytic reduction of nitrate to ammonia, *Nano Energy* 97 (2022), 107124.
- [13] T. Ren, K. Ren, M. Wang, M. Liu, Z. Wang, H. Wang, X. Li, L. Wang, Y. Xu, Concave-convex surface oxide layers over copper nanowires boost electrochemical nitrate-to-ammonia conversion, *Chem. Eng. J.* 426 (2021), 130759.
- [14] R. Jia, Y. Wang, C. Wang, Y. Ling, Y. Yu, B. Zhang, Boosting selective nitrate electroreduction to ammonium by constructing oxygen vacancies in TiO_2 , *ACS Catal.* 10 (2020) 3533–3540.
- [15] X. Zhang, Y. Wang, C. Liu, Y. Yu, S. Lu, B. Zhang, Recent advances in non-noble metal electrocatalysts for nitrate reduction, *Chem. Eng. J.* 403 (2021), 126269.
- [16] F. Zhou, C. Sun, Nitrate-to-ammonia conversion on Ru/Ni hydroxide hybrid through Zinc-nitrate fuel cell, *Small* 18 (2022), 2200436.
- [17] Z. Li, J. Liang, Q. Liu, L. Xie, L. Zhang, Y. Ren, L. Yue, N. Li, B. Tang, A.A. Alshehri, M.S. Hamdy, Y. Luo, Q. Kong, X. Sun, High-efficiency ammonia electrosynthesis via selective reduction of nitrate on ZnCo_2O_4 nanosheet array, *Mater. Today Phys.* 23 (2022), 100619.
- [18] Z. Deng, J. Liang, Q. Liu, C. Ma, L. Xie, L. Yue, Y. Ren, T. Li, Y. Luo, N. Li, B. Tang, A.A. Alshehri, I. Shakir, P.O. Agboola, S. Yan, B. Zheng, J. Du, Q. Kong, X. Sun, High-efficiency ammonia electrosynthesis on self-supported Co_2AlO_4 nanoarray in neutral media by selective reduction of nitrate, *Chem. Eng. J.* 45 (2022), 135104.
- [19] Q. Liu, L. Xie, J. Liang, Y. Ren, Y. Wang, L. Zhang, L. Yue, T. Li, Y. Luo, N. Li, B. Tang, Y. Liu, S. Gao, A.A. Alshehri, I. Shakir, P.O. Agboola, Q. Kong, Q. Wang, D. Ma, X. Sun, Ambient ammonia synthesis via electrochemical reduction of nitrate enabled by NiCo_2O_4 nanowire array, *Small* 18 (2022), 2106961.
- [20] H. Wang, D. Zhao, C. Liu, X. Fan, Z. Li, Y. Luo, D. Zheng, S. Sun, J. Chen, J. Zhang, Y. Liu, S. Gao, F. Gong, X. Sun, $\text{FeS}_2/\text{TiO}_2$ nanobelt array enabled high-efficiency electrocatalytic nitrate reduction to ammonia, *J. Mater. Chem. A* 10 (2022) 24462–24467.
- [21] Z. Deng, C. Ma, X. Fan, Z. Li, Y. Luo, S. Sun, D. Zheng, Q. Liu, J. Du, Q. Lu, B. Zheng, X. Sun, Construction of CoP/TiO_2 nanoarray for enhanced electrochemical nitrate reduction to ammonia, *Mater. Today Phys.* 28 (2022), 100854.
- [22] Y. Xu, Y. Wen, T. Ren, H. Yu, K. Deng, Z. Wang, X. Li, L. Wang, H. Wang, Engineering the surface chemical microenvironment over CuO nanowire arrays by polyaniline modification for efficient ammonia electrosynthesis from nitrate, *Appl. Catal. B: Environ.* 320 (2023), 121981.
- [23] Y. Gao, K. Huang, C. Yan, S. Li, H. Zhang, L. Cheng, F. Huang, Interfacial engineering of Cu- Fe_2O_3 nanotube arrays with built-in electric field and oxygen vacancies for boosting the electrocatalytic reduction of nitrates, *Mater. Adv.* 3 (2022) 7107–7115.
- [24] G. Wang, P. Shen, Y. Luo, X. Li, X. Xia, K. Chu, A vacancy engineered MnO_{2-x} electrocatalyst promotes nitrate electroreduction to ammonia, *Dalton Trans.* 51 (2022) 9206–9212.
- [25] X. Xu, L. Hu, Z. Li, L. Xie, S. Sun, L. Zhang, J. Li, Y. Luo, X. Yan, M.S. Hamdy, Q. Kong, X. Sun, Q. Liu, Oxygen vacancies in Co_3O_4 nanoarrays promote nitrate electroreduction for ammonia synthesis, *Sustain. Energy Fuels* 6 (2022) 4130–4136.
- [26] P. Shen, G. Wang, K. Chen, J. Kang, D. Ma, K. Chu, Selenium-vacancy-rich WSe_2 for nitrate electroreduction to ammonia, *J. Colloid Interf. Sci.* 629 (2023) 563–570.
- [27] Z. Deng, C. Ma, Z. Li, Y. Luo, L. Zhang, S. Sun, Q. Liu, J. Du, Q. Lu, B. Zheng, X. Sun, High-efficiency electrochemical nitrate reduction to ammonia on a Co_3O_4 nanoarray catalyst with cobalt vacancies, *ACS Appl. Mater. Interfaces* 14 (2022) 46595–46602.
- [28] P. Wei, J. Liang, Q. Liu, L. Xie, X. Tong, Y. Ren, T. Li, Y. Luo, N. Li, B. Tang, A. M. Asiri, M.S. Hamdy, Q. Kong, Z. Wang, X. Sun, Iron-doped cobalt oxide nanoarray for efficient electrocatalytic nitrate-to-ammonia conversion, *J. Colloid Interface Sci.* 615 (2022) 636–642.
- [29] Y. Luo, K. Chen, P. Shen, X. Li, X. Li, Y. Li, K. Chu, B-doped MoS_2 for nitrate electroreduction to ammonia, *J. Colloid Interface Sci.* 629 (2023) 950–957.
- [30] W. Zhong, Z. Gong, Z. He, N. Zhang, X. Kang, X. Mao, Y. Chen, Modulating surface oxygen species via facet engineering for efficient conversion of nitrate to ammonia, *J. Energy Chem.* 78 (2023) 211–221.
- [31] R. Zhang, Y. Guo, S. Zhang, D. Chen, Y. Zhao, Z. Huang, L. Ma, P. Li, Q. Yang, G. Liang, C. Zhi, Efficient ammonia electrosynthesis and energy conversion through a Zn-nitrate battery by Iron doping engineered nickel phosphide catalyst, *Adv. Energy Mater.* 12 (2022), 2103872.
- [32] Q. Wei, F. Xiong, S. Tan, L. Huang, E.H. Lan, B. Dunn, L. Mai, Porous one-dimensional nanomaterials: Design, fabrication and applications in electrochemical energy storage, *Adv. Mater.* 29 (2017), 1602300.
- [33] C. Chen, Y. Kang, Z. Huo, Z. Zhu, W. Huang, H.L. Xin, J.D. Snyder, D. Li, J. A. Herron, M. Mavrikakis, M. Chi, K.L. More, Y. Li, N.M. Markovic, G.A. Somorjai, P. Yang, V.R. Stamenkovic, Highly crystalline multimetallic nanoframes with three-dimensional electrocatalytic surfaces, *Science* 343 (2014) 1339–1343.
- [34] H.H. Li, S.H. Yu, Recent advances on controlled synthesis and engineering of hollow alloyed nanotubes for electrocatalysis, *Adv. Mater.* 31 (2019), 1803503.
- [35] L. Fan, Z. Xia, M. Xu, Y. Lu, Z. Li, 1D SnO_2 with wire-in-tube architectures for highly selective electrochemical reduction of CO_2 to C_1 products, *Adv. Funct. Mater.* 28 (2018), 1706289.

- [36] L. Yu, J.F. Yang, B.Y. Guan, Y. Lu, X.W.D. Lou, Hierarchical hollow nanoprism based on ultrathin Ni-Fe layered double hydroxide nanosheets with enhanced electrocatalytic activity towards oxygen evolution, *Angew. Chem. Int. Ed.* 57 (2018) 172–176.
- [37] Q. Li, F. Huang, S. Li, H. Zhang, X.Y. Yu, Oxygen vacancy engineering synergistic with surface hydrophilicity modification of hollow Ru doped CoNi-LDH nanotube arrays for boosting hydrogen evolution, *Small* 18 (2022), 2104323.
- [38] M. Jin, X. Zhang, M. Han, H. Wang, G. Wang, H. Zhang, Efficient electrochemical N₂ fixation by doped-oxygen-induced phosphorus vacancy defects on copper phosphide nanosheets, *J. Mater. Chem. A* 8 (2020) 5936–5942.
- [39] L. Wu, L. Yu, F. Zhang, B. McElhenny, D. Luo, A. Karim, S. Chen, Z. Ren, Heterogeneous bimetallic phosphide Ni₂P-Fe₂P as an efficient bifunctional catalyst for water/seawater splitting, *Adv. Funct. Mater.* 31 (2021), 2006484.
- [40] K. Wang, H. Xie, Y. Li, G. Wang, Z. Jin, Construction of CoP/Cu₃P/Ni₂P double S-scheme heterojunctions for improved photocatalytic hydrogen evolution, *J. Phys. Chem. C* 126 (2022) 6947–6959.
- [41] R. Sun, Y. Bai, Z. Bai, L. Peng, M. Luo, M. Qu, Y. Gao, Z. Wang, W. Sun, K. Sun, Phosphorus vacancies as effective polysulfide promoter for high-energy-density Lithium-Sulfur batteries, *Adv. Energy Mater.* 12 (2022), 2102739.
- [42] D. Yan, Y. Li, J. Huo, R. Chen, L. Dai, S. Wang, Defect chemistry of nonprecious-metal electrocatalysts for oxygen reactions, *Adv. Mater.* 29 (2017), 1606459.
- [43] J.J. Zhang, H.H. Wang, T.J. Zhao, K.X. Zhang, X. Wei, Z.D. Jiang, S.I. Hirano, X. H. Li, J.S. Chen, Oxygen vacancy engineering of Co₃O₄ nanocrystals through coupling with metal support for water oxidation, *ChemSusChem* 10 (2017) 2875–2879.
- [44] X. Luo, P. Ji, P. Wang, X. Tan, L. Chen, S. Mu, Spherical Ni₃S₂/Fe-NiP_x magic cube with ultrahigh water/seawater oxidation efficiency, *Adv. Sci.* 9 (2022), 2104846.
- [45] C. Yao, J. Li, Z. Zhang, C. Gou, Z. Zhang, G. Pan, J. Zhang, Hierarchical core-shell Co₂N/CoP embedded in N, P-doped carbon nanotubes as efficient oxygen reduction reaction catalysts for Zn-air batteries, *Small* 18 (2022), 2108094.
- [46] F.H. Saadi, A.I. Carim, W.S. Drisdell, S. Gul, J.H. Baricuatro, J. Yano, M.P. Soriaga, N.S. Lewis, Operando spectroscopic analysis of CoP films electrocatalyzing the hydrogen-evolution reaction, *J. Am. Chem. Soc.* 139 (2017) 12927–12930.
- [47] H. Zhou, F. Yu, J. Sun, R. He, S. Chen, C.W. Chu, Z. Ren, Highly active catalyst derived from a 3D foam of Fe(PO₃)₂/Ni₂P for extremely efficient water oxidation, *Proc. Natl. Acad. Sci. U. S. A.* 114 (2017) 5607–5611.
- [48] S. Tasleem, M. Tahir, Z.Y. Zakaria, Fabricating structured 2D Ti₃AlC₂ MAX dispersed TiO₂ heterostructure with Ni₂P as a cocatalyst for efficient photocatalytic H₂ production, *J. Alloy. Compd.* 842 (2020), 155752.
- [49] Z. Ye, Y. Jiang, L. Li, F. Wu, R. Chen, Synergetic anion vacancies and dense heterointerfaces into bimetal chalcogenide nanosheet arrays for boosting electrocatalysis sulfur conversion, *Adv. Mater.* 34 (2022), 2109552.
- [50] P. He, X.Y. Yu, X.W. Lou, Carbon-incorporated nickel-cobalt mixed metal phosphide nanoboxes with enhanced electrocatalytic activity for oxygen evolution, *Angew. Chem. Int. Ed.* 56 (2017) 3897–3900.
- [51] Z. Ran, C. Shu, Z. Hou, P. Hei, T. Yang, R. Liang, J. Li, J. Long, Phosphorus vacancies enriched Ni₂P nanosheets as efficient electrocatalyst for high-performance Li-O₂ batteries, *Electrochim. Acta* 337 (2020), 135795.
- [52] J. Duan, S. Chen, C.A. Ortiz-Ledon, M. Jaroniec, S.Z. Qiao, Phosphorus vacancies that boost electrocatalytic hydrogen evolution by two orders of magnitude, *Angew. Chem. Int. Ed.* 59 (2020) 8181–8186.
- [53] Z. Wang, J. Yang, W. Wang, F. Zhou, H. Zhou, Z. Xue, C. Xiong, Z.-Q. Yu, Y. Wu, Hollow cobalt-nickel phosphide nanocages for efficient electrochemical overall water splitting, *Sci. China Mater.* 64 (2021) 861–869.
- [54] C. Liu, G. Zhang, L. Yu, J. Qu, H. Liu, Oxygen doping to optimize atomic hydrogen binding energy on NiCoP for highly efficient hydrogen evolution, *Small* 14 (2018), 1800421.
- [55] X. Zhou, H. Gao, Y. Wang, Z. Liu, J. Lin, Y. Ding, P vacancies-enriched 3D hierarchical reduced cobalt phosphide as a precursor template for defect engineering for efficient water oxidation, *J. Mater. Chem. A* 6 (2018) 14939–14948.
- [56] Z. Ping, H. Fang, K. Wang, H. Zhang, S. Li, J. Chen, F. Huang, A universal Cl-PEDOT coating strategy based on oxidative chemical vapor deposition toward solar-driven multifunctional energy management, *Adv. Funct. Mater.* 32 (2022), 2208965.
- [57] X. Yang, Y. Luo, J. Li, H. Wang, Y. Song, J. Li, Z. Guo, Tuning mixed electronic/ionic conductivity of 2D CdPS₃ nanosheets as an anode material by synergistic intercalation and vacancy engineering, *Adv. Funct. Mater.* 32 (2022), 2112169.
- [58] L. Wan, W. Tian, N. Li, D. Chen, Q. Xu, H. Li, J. He, J. Lu, Hydrophilic porous PVDF membrane embedded with BaTiO₃ featuring controlled oxygen vacancies for piezocatalytic water cleaning, *Nano Energy* 94 (2022), 106930.
- [59] N. Kitiphatiboon, S. Sirisomboonchai, M. Chen, S. Li, X. Li, J. Wang, X. Hao, A. Abudula, G. Guan, Facile fabrication of O vacancy rich CuVO_x nanobelt@NiO nanosheet array for hydrogen evolution reaction, *Electrochim. Acta* 405 (2022), 139623.
- [60] K. Xu, Y. Sun, X. Li, Z. Zhao, Y. Zhang, C. Li, H.J. Fan, Fluorine-induced dual defects in cobalt phosphide nanosheets enhance hydrogen evolution reaction activity, *ACS Mater. Lett.* 2 (2020) 736–743.
- [61] M. Nazemia, M.A. El-Sayed, Plasmon-enhanced photo(electro)chemical nitrogen fixation under ambient conditions using visible light responsive hybrid hollow Au-Ag₂O nanocages, *Nano Energy* 63 (2019), 103886.
- [62] X. Fu, X. Zhao, X. Hu, K. He, Y. Yu, T. Li, Q. Tu, X. Qian, Q. Yue, M.R. Wasielewski, Y. Kang, Alternative route for electrochemical ammonia synthesis by reduction of nitrate on copper nanosheets, *Appl. Mater. Today* 19 (2020), 100620.
- [63] Y. Wang, W. Zhou, R. Jia, Y. Yu, B. Zhang, Unveiling the activity origin of a copper-based electrocatalyst for selective nitrate reduction to ammonia, *Angew. Chem. Int. Ed.* 59 (2020) 5350–5354.
- [64] L. Zhang, L.X. Ding, G.F. Chen, X. Yang, H. Wang, Ammonia synthesis under ambient conditions: selective electroreduction of dinitrogen to ammonia on black phosphorus nanosheets, *Angew. Chem. Int. Ed.* 58 (2019) 2612–2616.
- [65] Y. Guo, J. Liu, Q. Yang, P. Khemthong, Z. Huang, Y. Zhao, Z. Chen, B. Dong, X.-Z. Fu, J.-L. Luo, C. Zhi, Regulating nitrogenous adsorption and desorption on Pd clusters by the acetylene linkages of hydrogen substituted graphdiyne for efficient electrocatalytic ammonia synthesis, *Nano Energy* 86 (2021), 106099.
- [66] F. Lei, K. Li, M. Yang, J. Yu, M. Xu, Y. Zhang, J. Xie, P. Hao, G. Cui, B. Tang, Electrochemical reduction of nitrate on silver surface and an in situ Raman spectroscopy study, *Inorg. Chem. Front.* 3 (2022) 2734–2740.